A&A, 706, A226 (2026)
https://doi.org/10.1051/0004-6361/202557682

Astronomy & Astrophysics

X-ray and radio observations of the AMXP MAXI J1957+032 covering the 2022–2025 outbursts

Zhaosheng Li[1,⋆], Lucien Kuiper[2], Yuanyue Pan[1], Renxin Xu[3,4], Mingyu Ge[5], Shanshan Weng[6], Long Peng[7], Wenhui Yu[7], Yue Huang[5], Liang Zhang[5], Liming Song[5,8], Sergey V. Molkov[9], Alexander A. Lutovinov[9], Shu Zhang[5], and Shuang-Nan Zhang[5]

[1] School of Science, Qingdao University of Technology, Qingdao 266525, PR China
[2] SRON – Space Research Organisation Netherlands, Niels Bohrweg 4, 2333 CA Leiden, The Netherlands
[3] Department of Astronomy, School of Physics, Peking University, Beijing 100871, PR China
[4] Kavli Institute for Astronomy and Astrophysics, Peking University, Beijing 100871, PR China
[5] Key Laboratory of Particle Astrophysics, Institute of High Energy Physics, Chinese Academy of Sciences, 19B Yuquan Road, Beijing 100049, China
[6] Department of Physics and Institute of Theoretical Physics, Nanjing Normal University, Nanjing 210023, PR China
[7] Key Laboratory of Stars and Interstellar Medium, Xiangtan University, Xiangtan 411105, Hunan, PR China
[8] University of Chinese Academy of Sciences, Beijing 100049, China
[9] Space Research Institute, Russian Academy of Sciences, Profsoyuznaya 84/32, 117997 Moscow, Russia

Received 14 October 2025 / Accepted 29 December 2025

ABSTRACT

We presented a comprehensive multi-epoch timing and multiwavelength analysis of the accreting millisecond X-ray pulsar MAXI J1957+032, covering two major outbursts in 2022 and 2025. By reanalyzing the 2022 outburst data from the *Neutron Star Interior Composition Explorer* (NICER), we found the spin frequency and orbital parameters from the observations in 0.3–5 keV. For the 2025 outburst, we reported the detection of pulsations with the *Einstein Probe* (EP). Based on the ∼3-year baseline between these two outbursts, we measured a significant long-term spin-down rate of $\dot{\nu} = (-5.73 \pm 0.28) \times 10^{-14}$ Hz s^{-1}. Assuming that the quiescent spin-down is driven by magnetic dipole radiation, we inferred a spin-down luminosity of $L \approx 1.1 \times 10^{36}$ erg s^{-1} and a surface dipolar magnetic field of $B \approx (7.3–10.4) \times 10^8$ G. Furthermore, we conducted a deep radio pulsation search with the *Five-hundred-meter Aperture Spherical radio Telescope* (FAST) during the X-ray quiescent state in 2024, resulting in a non-detection with a 7σ flux density upper limit of 12.3 µJy. This corresponds to a radio efficiency upper limit of $\xi < 2.8 \times 10^{-10}$, which is significantly lower than that of typical millisecond pulsars with a similar spin-down power. This profound radio pulsation faintness can be explained by two primary scenarios: either a geometric effect, wherein the pulsar's radio beam is directed away from our line of sight, or a physical suppression of the emission mechanism, potentially caused by a persistent low-level accretion flow during the X-ray quiescent state.

Key words. accretion, accretion disks – binaries: general – stars: neutron – pulsars: individual: MAXI J1957+032

1. Introduction

The transient X-ray source MAXI J1957+032 was first discovered on May 11, 2015, by the *Monitor of All-sky X-ray Image* (MAXI), which detected a faint and short-lived outburst (Negoro et al. 2015). Coincident with an independent discovery by *INTEGRAL* (Cherepashchuk et al. 2015), rapid follow-up observations with the *Neil Gehrels Swift Observatory* and the GROND optical telescope quickly localized the source and confirmed its nature as a fast transient, with the initial outburst decaying on a timescale of less than a day (Molkov et al. 2015; Rau et al. 2015).

Since its discovery, MAXI J1957+032 has established itself as a prolific recurrent transient, and its activity has become well characterized. The source typically underwent outbursts that were consistently short, lasting only a few days, and relatively dim, with peak luminosities of a few tens of milli-Crab. This pattern was observed in subsequent outbursts in October 2015 (Sugimoto et al. 2015) and January 2016 (Tanaka et al. 2016). A notable exception occurred in September 2016, when the source exhibited an outburst that was approximately 20 times brighter and spectrally harder than previously seen (Kennea et al. 2016). An observation of this bright outburst with *Chandra* provided the sub-arcsecond localization for the source, which confirmed the association with the optical counterpart and revealed significant spectral evolution during the outburst decay (Chakrabarty et al. 2016). A comprehensive analysis of these first four outbursts was presented by Mata Sánchez et al. (2017). They highlighted that the combination of short outburst durations, frequent recurrence, and a featureless blue optical spectrum was strongly reminiscent of the known accreting millisecond X-ray pulsar (AMXP) population. Based on these characteristics, they were the first to propose that MAXI J1957+032 was an AMXP candidate. Furthermore, by assuming a peak outburst luminosity typical for AMXPs (∼1% of the Eddington limit), they estimated a source distance of approximately 5–6 kpc, which was refined to 5±2 kpc by Ravi (2017).

This AMXP prediction was definitively confirmed during the source's 2022 outburst (Negoro et al. 2022), when the *Neutron Star Interior Composition Explorer* (NICER) discovered

⋆ Corresponding author: lizhaosheng@xtu.edu.cn

coherent pulsations at ∼314 Hz. This detection firmly identified MAXI J1957+032 as an AMXP in a 1-hour ultracompact binary orbit (Sanna et al. 2022). Radio observations during this outburst yielded a non-detection, suggesting that the source was radio-quiet while active in X-rays (van den Eijnden et al. 2022). Most recently, a new outburst in May 2025 was discovered independently by Einstein Probe (EP)/WXT and MAXI (Sun et al. 2025; Negoro et al. 2025). Highlighting its unique rapid follow-up capabilities, EP detected the ∼314 Hz pulsations during this outburst (Li et al. 2025b). This crucial detection provided a second, independent timing solution separated by a baseline of approximately three years.

In this work we report on the analysis of MAXI J1957+032 data from NICER observations performed during its 2022 and 2025 outbursts, and from EP, *Insight*-HXMT, and NuSTAR observations during its 2025 outburst, as well as from FAST radio observations during the X-ray quiescent state between these two outbursts. In Sect. 2, we introduce the observations and data analysis. The timing and spectral results are reported in Sects. 3 and 4, respectively. We discuss our main findings in Sect. 5.

2. X-ray and radio observations

2.1. Einstein Probe

EP was launched on January 9, 2024, equipped with WXT and FXT (Yuan et al. 2025). EP has the capability to detect transients and perform rapid follow-up observations with excellent timing and spectral resolutions. FXT, including FXT-A and FXT-B, can operate in timing mode (TM), full frame (FF) mode, and partial window (PW) mode (Chen et al. 2020a). The timing resolution of TM is 23.68 µs (Zhao et al. 2025), which has been verified by the joint observations with NICER for the AMXP SRGA J144459.2−604207 (Li et al. 2025a).

On May 6, 2025, EP/WFT reported an outburst from MAXI J1957+032. EP/FXT promptly triggered the target-of-opportunity (ToO) observations (Sun et al. 2025). Six observations have been carried out between MJD UTC 60801.88–60807.26 (see Table 1). We processed EP/FXT observations using the tool `fxtchain`. The source light curves, spectra, ancillary response files (ARFs), and response matrix files (RMFs) were extracted from a circle region centered on the source position with a radius of 100″, while the background spectra were from a nearby source-free region with the same radius. For the TM data we barycentered the event times using the tool `fxtbary`, adopting the JPL DE421 Solar System ephemeris and the source coordinates as listed in Table 3.

2.2. NICER

NICER (Gendreau et al. 2016) observed MAXI J1957+032 with the Obs. ID. 5202840101–5202840106 and 8202840101–8202840105 during its 2022 and 2025 outbursts, respectively. The results of the 2022 outburst observations have been reported by Sanna et al. (2022). To perform a comprehensive coherent timing study, we analyzed all available NICER observations from both outbursts. The data were processed with HEASOFT version 6.33 and the NICER software NICERDAS version v12. We focused on the data from the calibrated unfiltered (UFA) event files. To identify and reject the time intervals of high background, we first extracted light curves in the 12–15 keV band, where the effective area for X-ray photons is negligible and events are dominated by charged particle interactions. Time intervals where this rate exceeded 5 cnt s^{-1} were identified as particle flares and excluded. Subsequently, we applied a count rate screening in the energy band of interest, retaining only time intervals with count rates less than 10 cnt s^{-1}. The UFA events were barycenter-corrected using the `barycor` tool and the JPL DE421 Solar System ephemeris.

Table 1. X-ray observations of MAXI J1957+032 for the 2022 and 2025 outbursts.

Mission	Obs. ID	Instrument	Exposure (ks)
2022 outburst			
NICER	5202840101	XTI	2.07
	5202840102	XTI	3.46
	5202840103	XTI	9.00
	5202840104	XTI	5.35
	5202840105	XTI	2.43
	5202840106	XTI	0.23
2025 outburst			
NuSTAR	90501329001	FPMA/FPMB	46.47
NICER	8202840101	XTI	0.91
	8202840102	XTI	1.12
	8202840103	XTI	0
	8202840104	XTI	0.22
	8202840105	XTI	0.10
Insight-HXMT	P0704848001	LE/ME/HE	3.43/6.52/3.76
EP	01709175213	A(PW)/B(FF)	4.10
	06800000586	A(TM)/B(TM)	3.02
	06800000587	A(TM)/B(PW)	3.01
	06800000589	A(TM)/B(PW)	1.78
	06800000595	A(TM)/B(PW)	3.00
	06800000597	A(PW)/B(PW)	4.27

2.3. Insight-HXMT

During the 2025 outburst, we triggered the *Insight*-HXMT (Zhang et al. 2020; Cao et al. 2020; Liu et al. 2020) ToO observations during MJD 60805.08–60805.48. The data were processed with the tool `hpipeline`, and the filtered exposure times for the low-energy (LE; Chen et al. 2020b), middle-energy (ME; Cao et al. 2020), and high-energy (HE; Liu et al. 2020) telescopes are presented in Table 1. The events of ME and HE, generated from `mescreen` and `hescreen`, respectively, were barycentered using `hxbary`.

2.4. NuSTAR

We also analyzed an archival NuSTAR (Harrison et al. 2013) observation (Obs. ID 90501329001) of MAXI J1957+032 taken during the 2025 outburst. The observation was performed over the MJD range 60809.57–60810.64, resulting in a total exposure of 46.47 ks. Data from both the FPMA and FPMB were processed separately using the standard NuSTAR pipeline tool `nupipeline`. However, no significant emission from MAXI J1957+032 was detected in the data from either module. Consequently, these NuSTAR data are not considered further in our subsequent analysis.

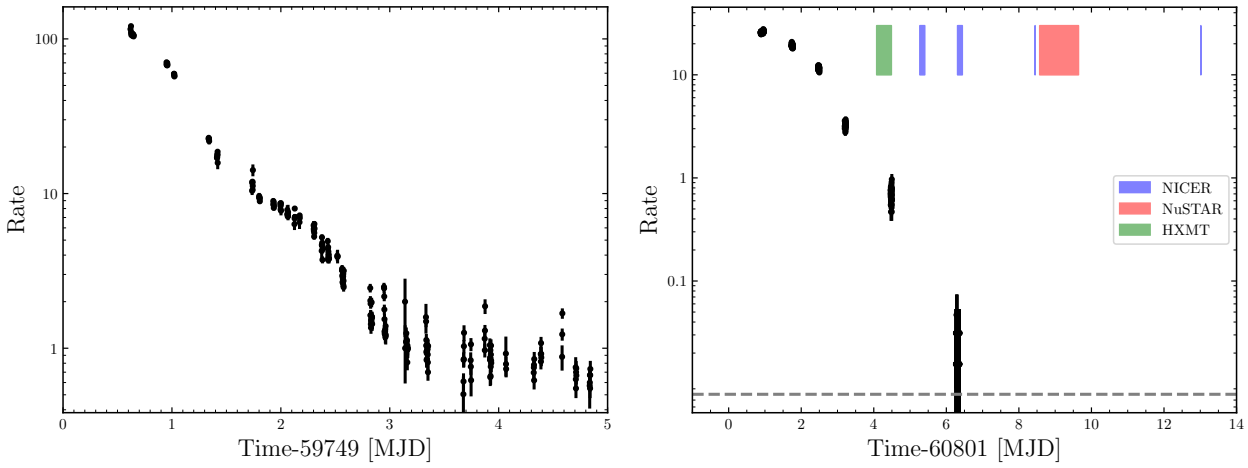

Fig. 1. Light curves of MAXI J1957+032 from NICER (left panel, 0.5–10 keV), and EP (right panel, 0.5–10 keV) during its 2022 and 2025 outbursts, respectively. The vertical axes display the total count rate (source plus background) in units of counts per second on a logarithmic scale. In the right panel, the shaded rectangles mark the observational intervals of NICER (blue), NuSTAR (red), and *Insight*-HXMT (green). The dashed horizontal line indicates the background level for the EP observations.

2.5. The outburst light curve

The 2025 outburst light curve of MAXI J1957+032 (EP/FXT based) is presented in the right panel of Fig. 1 and for comparison the 2022 outburst light curve (NICER based) is shown in the left panel of Fig. 1. The right panel of Fig. 1 also shows the observation windows of various other X-ray missions. The EP/FXT observations began around MJD 60802.5, with a count rate of approximately 28 cnt s^{-1}. While the rise of the outburst was not covered by these data, the subsequent evolution was characterized by a rapid and steep decay, with the source returning to a near-quiescent state by MJD 60806. Similar features have also been shown in the 2022 outburst (see the left panel in Fig. 1). The ∼4-day duration of this decay phase is consistent with the short-duration outburst behavior that is typical for this source. The *Insight*-HXMT, NICER, and NuSTAR observations were carried out during the very end of the outburst decay phase or even during the subsequent quiescent state. No type I X-ray bursts were found during these two outbursts.

2.6. FAST

In 2024, we conducted four FAST observations of MAXI J1957+032, with a total duration of 1.67 h. The observations were made using the 19-beam *L*-band receiver of FAST in the tracking mode, covering the 1.05–1.45 GHz frequency band. The data were recorded in the PSRFITS format (Hotan et al. 2004), with 8-bit resolution, 4096 frequency channels, four polarizations, and a sampling time of 49.152 µs (Jiang et al. 2020).

We performed a pulsar search using `PRESTO`[1] (Ransom 2001). The optimal dedispersion strategies were determined using the script `DDplan.py`, covering dispersion measure up to 1000 pc cm^{-3}, and applied the acceleration search with an integration time (t_{int} ∼ 6 min) spanning 10% of the orbital period. The `accelsearch` routine was employed with parameter z_{max} = 200, which represents the maximum number of Fourier bins that the highest harmonic can drift linearly in the power spectrum. No significant radio pulsations were detected. The upper limit on the source flux density, i.e., the minimum detectable flux density, S_{min}, is given by (van Leeuwen & Stappers 2010)

$$S_{min} = \frac{(S/N)\beta T_{sys}}{G(n_p t_{int}\Delta F)^{1/2}}\left(\frac{W}{P-W}\right)^{1/2}, \quad (1)$$

where S/N is the threshold in the signal-to-noise ratio for the pulsar detection, n_p is the number of polarizations, β is the sensitivity degradation factor, T_{int} is the integration time, ΔF is the observing frequency bandwidth, P and W are the pulsar spin period and pulse width, respectively, G is the telescope gain, and T_{sys} is the system temperature. For our observations, the G and T_{sys} values, which vary with the zenith angle, are listed in Table 2. We used β = 1, S/N = 7, n_p = 2, ΔF = 400 MHz, and W/P = 0.3. Adopting these parameters, the 7σ flux density upper limit for each observation was constrained to 12.3−16.3 µJy (see Table 2).

Table 2. Details of FAST observations and data reduction.

Obs. No.	Obs. MJD	Length (min)	G (K Jy^{-1})	T_{sys} (K)	Sensitivity (µJy)
01	60335.25	30	14.6	29.3	16.3
02	60365.10	30	16.2	24.4	12.3
03	60394.98	20	16.1	27.6	14.0
04	60424.91	20	16.2	26.3	13.2

3. Timing results

3.1. The 2022 outburst

We reanalyzed the NICER data from the 2022 outburst of MAXI J1957+032, originally presented by Sanna et al. (2022). Their timing solution provided an orbital and spin ephemeris for the source, yielding a spin frequency, ν, of 313.64374049(22) Hz. However, they introduced a phase jump of ∼0.2 around MJD 59750.2, increasing the number of free parameters from 5 to 7.

To investigate the timing solution for this dataset we employed a 4D optimization scheme based on a downhill `SIMPLEX` algorithm (see e.g., De Falco et al. 2017; Li et al.

[1] https://github.com/scottransom/presto

Table 3. Orbital and spin parameters of MAXI J1957+032 derived in this work from a 4D optimization scheme using NICER 0.5–10 keV data for the 2022 outburst and EP 0.5–10 keV data for the 2025 outburst.

Parameter	Values
α_{2000} [a]	$19^{\rm h}56^{\rm m}39\overset{\rm s}{.}11$
δ_{2000} [a]	$03°26'43\overset{''}{.}7$
e	0 (fixed)
2025 outburst: EP	
$P_{\rm orb}$ (s)	3652.95(43)
$a_{\rm x} \sin i$ (lt-s)	0.013 85(12)
$T_{\rm asc}$ (MJD, TDB)	60802.746 344(60)
Validity range (MJD, TDB)	60802–60807
t_0 (Epoch, MJD, TDB)	60804
ν (Hz)	313.643 736 8(7)
JPL Ephemeris	DE421
2022 outburst: NICER	
$P_{\rm orb}$ (s)	3652.94(15)
$a_{\rm x} \sin i$ (lt-s)	0.013 80(7)
$T_{\rm asc}$ (MJD, TDB)	59749.633 151(43)
Validity range (MJD, TDB)	59749–59755
t_0 (Epoch, MJD, TDB)	59752.0
ν (Hz)	313.643 741 98(24)
JPL Ephemeris	DE421

Notes. [a]The position used in the barycentering process (Chakrabarty et al. 2016).

2021, 2023 for the earlier 3D version, and Li et al. 2024, 2025a for the current 4D version of the method). This method was designed to efficiently locate the maximum of the Z_3^2 test statistic by simultaneously optimizing the spin frequency, ν, the orbital period, $P_{\rm orb}$, the projected semimajor axis, $a_x \sin i$, and the time of the ascending node, $T_{\rm asc}$ (assuming a circular orbit; four free parameters). We used the parameters from Sanna et al. (2022) as initial values for our optimization routine.

Our analysis resulted in an alternative, equivalent timing solution, with the parameters presented in Table 3. Our derived values for $P_{\rm orb}$, $a_x \sin i$, and $T_{\rm asc}$ are all consistent with the results of Sanna et al. (2022) at the 1σ confidence level. However, we measure a spin frequency of $\nu = 313.64374198(24)$ Hz, which differs from Sanna et al. (2022) by approximately 6σ. Alternatively, if we searched for the optimum spin frequency of the first NICER observation and the remaining five observations separately, i.e., before and after their introduced phase jump, we obtained for both sets the same value for the spin frequency as is reported in Sanna et al. (2022).

3.2. The 2025 outburst

We analyzed observations from multiple X-ray missions during the 2025 outburst, including NICER, NuSTAR, *Insight*-HXMT, and EP. We performed separate searches for coherent pulsations in the datasets from each of the four instruments. For each dataset, we employed a method similar to that applied to the 2022 outburst data, using a downhill `SIMPLEX` algorithm to optimize the spin and orbital parameters by maximizing the Z_3^2 statistic.

No significant pulsations were detected from MAXI J1957+032 in the NICER, NuSTAR, or *Insight*-HXMT observations. This can be explained because their observation windows miss the ON state of the outburst (see right panel of Fig. 1). In contrast, EP successfully monitored the source during the main activity of the outburst. We performed a timing analysis of the EP data taken in TM during MJD 60802.73–60805.47 with a total exposure time of 13.79 ks. Our independent search of the EP data yielded a strong detection with a Z_3^2 statistic value of approximately 197 (13.2σ). The resulting best solution for the 2025 outburst is presented in Table 3.

We compared these new parameters to those from our globally optimized solution for the 2022 NICER data. The orbital period, $P_{\rm orb}$, and the projected semimajor axis, $a_x \sin i$, from the 2025 outburst are fully consistent with our results from the 2022 outburst within their 1σ uncertainties. The newly measured time of the ascending node, $T_{\rm asc}$, of 60802.746344(60) and spin frequency, ν, of 313.6437368(7) Hz at a reference epoch, t_0, of 60802.0 MJD – separated from the 2022 observations by approximately three years – provide a long baseline that is useful for studying the long-term evolution of the pulsar's spin frequency (see Sect. 5.1).

3.3. The pulse profile morphology

Using the orbital parameters listed in Table 3, we corrected the barycentered event times from NICER and EP observations for the periodic orbital motion effects. For the 2022 outburst, we obtained after pulse-phase folding pulse-phase distributions (pulse-profiles) for the following energy ranges: 0.3–1.0, 1.0–2.0, 2.0–5.0, and 5.0–10 keV (see the left panels in Fig. 2). No significant pulsed emission was detected above 5 keV. The folded profile in this band is consistent with Poisson noise, and we place a 3σ upper limit on the pulsed amplitude of 4.6%.

For the 2025 outburst, we folded the EP timing data in the same energy ranges as the 2022 outburst (see the right panels of Fig. 2). The pulsations have now been detected across the whole energy band up to ~10 keV, indicating that the pulsed emission is harder than the 2022 outburst emission. After phase-aligning the profiles from both epochs by simple cross-correlation for a direct comparison, we found that the overall pulse shape is remarkably similar. The profiles from both the 2022 and 2025 outbursts were quite comparable, each showing a main peak at a phase of ~0.4 and a secondary peak at a phase of ~0. If the pulsed emission is produced from hot spot(s) at the magnetic pole(s), it suggests that the geometrical configuration between the magnetic pole, spin axis, and observer's viewing angle has not changed significantly between 2022 and 2025.

We also obtained time-resolved pulse profiles for the 2022 and 2025 outbursts to study the evolution of the pulse morphology. The time intervals for these profiles were defined based on the segmentation of the individual observation blocks. Specifically, the four panels on the left side of Fig. 3(a–d) correspond directly to the first four distinct NICER observations during the 2022 outburst. Similarly, for the 2025 outburst observed by EP, the four panels on the right (e–h) correspond directly to the observations 06800000586, 06800000587, 06800000589, and 06800000595, respectively, where TM mode data were available.

No significant pulsations have been detected in the time intervals of panels (d) and (g) in Fig. 3. Notably, for the interval corresponding to panel (g) (Obs. 3; MJD 60804.201–60804.235), the detection significance was only 2.5σ. This non-detection is intriguing because the total count rate during this observation was approximately 2.5 times higher than in the subsequent EP observation (Obs. 4; panel h), where pulsations were significantly detected (5.7σ). This behavior is likely

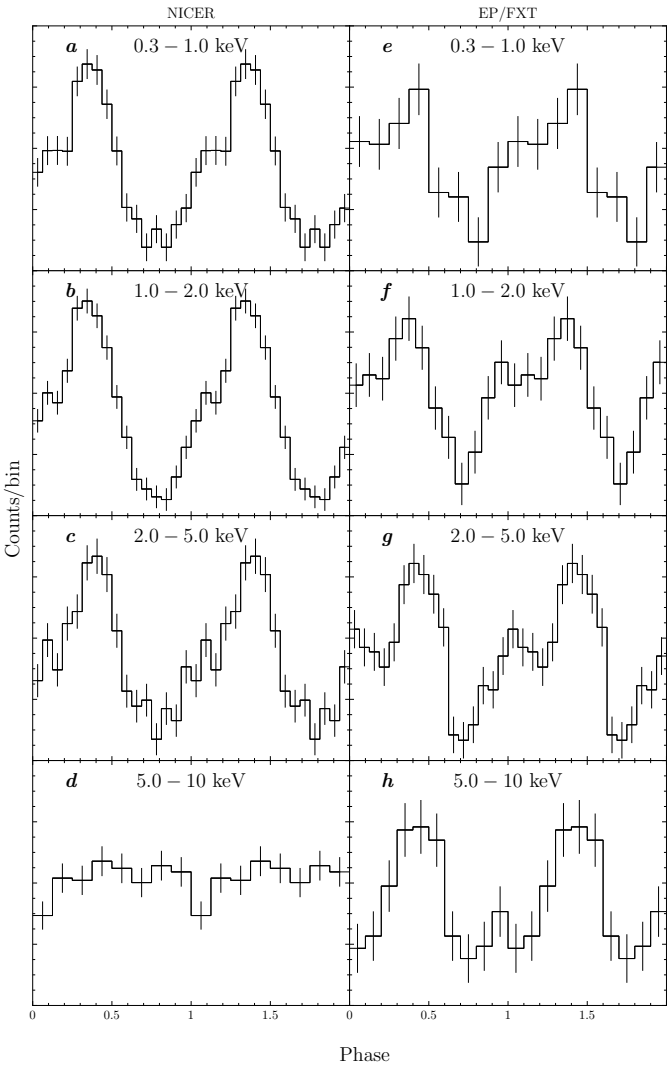

Fig. 2. Energy-resolved pulse profiles of MAXI J1957+032 during its 2022 outburst (left panels, a–d; 0.3−10 keV, observed with NICER) and 2025 outburst (right panels, e–h; 0.3−10 keV, observed with EP/FXT). Above 5 keV, the pulsed emission was undetectable in the 2022 outburst, but significant in the 2025 outburst. We show two cycles for clarity, while the error bars represent 1σ errors.

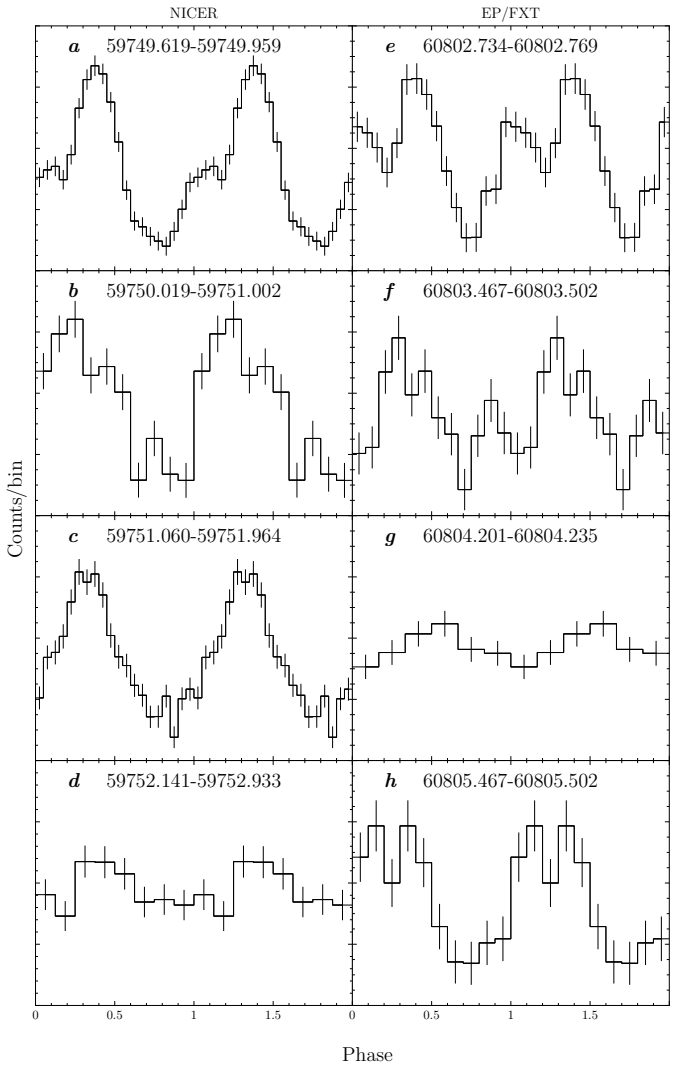

Fig. 3. Time-resolved pulse profiles of MAXI J1957+032 during its 2022 outburst (left panels, a–d; 0.3−5 keV, observed with NICER) and its 2025 outburst (right panels, e–h; 0.3−10 keV, observed with EP/FXT). We show two cycles for clarity, while the error bars represent 1σ errors. The time intervals in MJD are shown in the middle of the panels.

indicative of pulse intermittency, a phenomenon observed in other AMXPs such as IGR J17498–2921 (Li et al. 2024), SAX J1748.9–2021 (Altamirano et al. 2008), and HETE J1900.1–2455 (Galloway et al. 2007), possibly in combination with an intrinsic evolution of the pulsed fraction as the outburst decays (see e.g., Sanna et al. 2022, Fig. 1 for the 2022 outburst).

For the 2022 outburst observed by NICER, the profile initially exhibits a main peak accompanied by a shoulder in panel (a), which then transited into a more defined single-peaked structure in panels (b)–(c). A similar evolutionary pattern was observed for the 2025 data from EP/FXT, where the initial profiles in panels (e) and (f) also showed a main peak with a shoulder, before evolving into a single-peaked profile in panel (h). Moreover, beyond the changes in shape within each outburst, the phase of the main peak also clearly shifted during these two outbursts. This significant and complex evolution of the pulse morphology prevents us from performing a reliable time-of-arrival (TOA) analysis as has been done for other AMXPs that exhibit more stable pulse profiles (see e.g., Li et al. 2023, 2024, 2025a).

4. Spectral analysis

We performed a spectral analysis of the 2025 outburst using the data collected by EP/FXT. For our analysis, we prioritized data from the PW mode when available. For the observation for which PW mode data was not available (Obs. ID 06800000586), we used data from the TM. The spectra from individual observations were extracted, and fit in the 0.5–10 keV range using `XSPEC` version 12.14.1 (Arnaud 1996), adopting the `tbabs*powerlaw` model with abundances from Wilms et al. (2000). The free parameters are the hydrogen column density for `tbabs`, and the power-law index, Γ, and normalization.

This model provided an acceptable description of the spectra, with the best-fit reduced χ^2, $\chi^2_\nu \sim 0.9-1.6$. The parameters for the best fit are listed in Table 4. No significant trends are visible in the residuals (see Fig. 4). The analysis reveals a clear and significant spectral evolution throughout the outburst decay. The hydrogen column density, $N_{\rm H}$, remained low with best-fit values in the range of $(1-3) \times 10^{21}$ cm^{-2}. In the initial obser-

Table 4. Best-fit spectral parameters for different EP observations performed during the 2025 outburst of MAXI J1957+032.

Obs. ID	$N_{\rm H}$ (10^{22} cm^{-2})	Γ	Unabsorbed Flux (10^{-10} erg cm^{-2} s^{-1})	χ^2/d.o.f. (χ^2_ν)
01709175213	0.14 ± 0.01	1.87 ± 0.02	6.73 ± 0.05	119.4/74 (1.61)
06800000586	0.22 ± 0.02	1.99 ± 0.03	5.29 ± 0.06	97.7/96 (1.02)
06800000587	0.31 ± 0.03	2.28 ± 0.04	2.99 ± 0.07	78.8/68 (1.16)
06800000589	0.31 ± 0.02	2.63 ± 0.07	0.79 ± 0.03	97.6/66 (1.48)
06800000595	0.34 ± 0.05	3.27 ± 0.22	0.18 ± 0.02	52.8/60 (0.88)

Notes. The spectra were fit with the `tbabs*powerlaw` model for the 0.5–10 keV range. The unabsorbed fluxes in 0.5–10 keV are also reported. Errors are quoted at the 1σ confidence level.

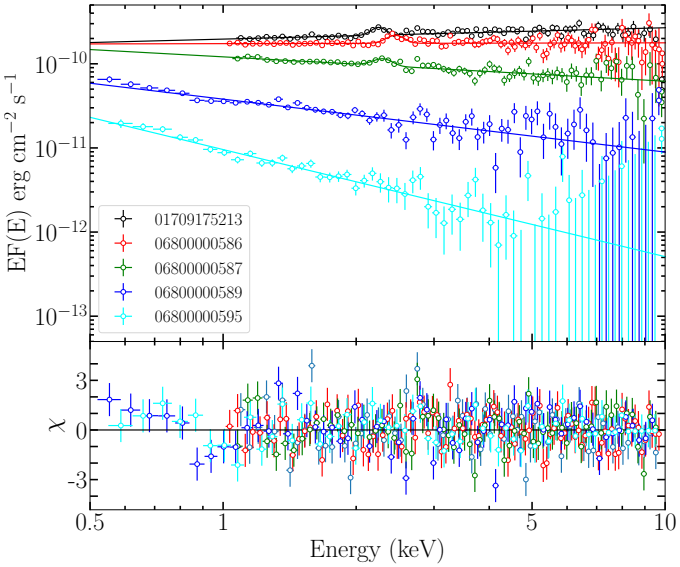

Fig. 4. Unfolded spectra and the best-fit models of the first five EP observations. For the first three observations, an instrumental Gaussian component is needed. Moreover, these spectra show strong excess below 1 keV, and are thus ignored.

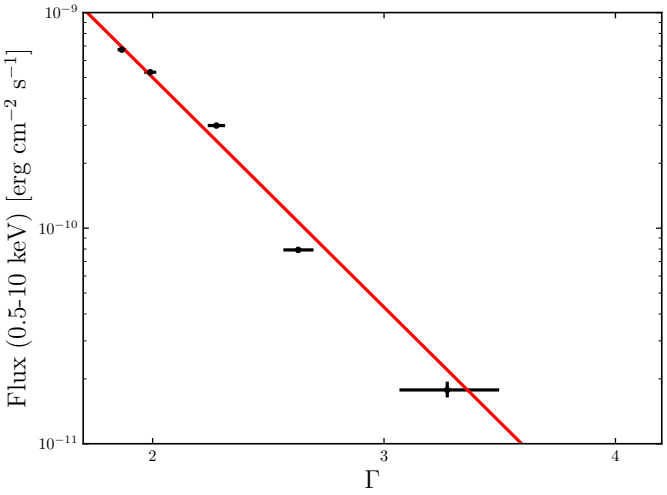

Fig. 5. Relation between the unabsorbed flux in 0.5–10 keV and the power law index, Γ. The red line represents the best fit, $F_X \sim \Gamma^{-(2.5\pm0.3)}$.

vation, the source was brightest with an unabsorbed 0.5–10 keV flux of $\sim 6.7 \times 10^{-10}$ erg s^{-1} cm^{-2}, and the spectrum was correspondingly hard, with a power-law photon index of $\Gamma \sim 1.87$. Over the subsequent days, the flux decayed by a factor of more than 30. This decay was accompanied by a systematic softening of the spectrum, with the photon index steepening to a final measured value of $\Gamma \sim 3.27$ in the last significant detection, which had a flux of $\sim 1.8 \times 10^{-11}$ erg s^{-1} cm^{-2}, see Fig. 4. Moreover, this correlation can be well described as $F_X \sim \Gamma^{-(2.5\pm0.3)}$; see Fig. 5. This trend of spectral softening with decreasing luminosity is consistent with the behavior observed in previous outbursts of this source (Mata Sánchez et al. 2017) and matches the evolution reported by Sanna et al. (2026) based on *Swift* monitoring of the 2025 outburst. Similar spectral evolution has also been reported for other AMXPs such as SAX J1808.4–3658 (Campana et al. 2008).

We note that during the first three observations, when the source was brightest, a narrow residual feature was consistently observed around 2.4 keV. This feature was well modeled by including a Gaussian component in the model. We attribute this feature to an instrumental origin, likely related to calibration uncertainties. Moreover, these spectra showed some excess below 1 keV, a feature that was notably absent in the 2022 dataset (Sanna et al. 2022), which was ignored in our analysis. The final observation was consistent with a non-detection and yielded only a weak constraint on the spectral parameters.

5. Discussion

In this work we have presented a comprehensive multiwavelength analysis of the AMXP MAXI J1957+032, covering its major outbursts in 2022 and 2025, as well as the intervening quiescent period. We have established high-precision timing solutions for these two distinct epochs, characterized the spectral evolution during the 2025 outburst, and placed a tight constraint on the source's radio emission during X-ray quiescence.

For the 2022 outburst, our reanalysis of the NICER data using a robust 4D optimization algorithm yielded a globally optimized timing solution. This newly derived ephemeris provided an independent and comparable solution to the one obtained by Sanna et al. (2022) without the introduction of any phase jump at a certain epoch (i.e., adding two more fit parameters). For the 2025 outburst, we reported a pulsation detection of 13.2σ from this source with EP. The analysis of this unique dataset provided a new timing solution for a second epoch, which was crucial as other X-ray missions did not detect pulsations during this event. Furthermore, our analysis of the EP/FXT spectra from the 2025 outburst revealed a clear spectral evolution, with the power-law photon index softening from $\Gamma \sim 1.9$ to $\Gamma \sim 3.3$ as the outburst decayed, a behavior that is characteristic of AMXPs. The successful acquisition of the 2025 outburst timing parameters is the

key result that enables the investigation of the long-term spin behavior of the system.

It is worth noting that while this manuscript was under review, an independent study by Sanna et al. (2026) appeared, reporting on the 2025 outburst using data from XMM-Newton. A comparison of the timing solutions reveals that the orbital parameters derived from XMM-Newton are highly consistent with our EP results within 1σ, and the measured spin frequencies are consistent within $\sim 2\sigma$.

5.1. Long-term spin-down rate

By combining the spin frequency measured during the 2022 outburst, $\nu_{2022} = 313.643\,741\,98(24)$ Hz, with that of the 2025 outburst, $\nu_{2025} = 313.643\,736\,8(7)$ Hz, we can constrain the long-term spin evolution of the pulsar. We define a quiescent baseline from the end of the 2022 outburst (MJD 59755) to the beginning of the 2025 outburst (MJD 60802). Assuming a constant spin-down during this interval, we calculated an average spin frequency derivative of $\dot{\nu} = (-5.73 \pm 0.28) \times 10^{-14}\,\mathrm{Hz\,s^{-1}}$. If this spin-down rate during the quiescent state is caused by (rotating) magnetic dipole emission, the magnetic dipole moment is (Spitkovsky 2006; Riggio et al. 2011)

$$\mu_{26} = 26.15 \times (1 + \sin^2\theta)^{-1/2} I_{45}^{1/2} \nu_2^{-3/2} (-\dot{\nu}_{-14})^{1/2}, \quad (2)$$

where θ is the angle between the rotation and magnetic axes, I_{45} is the NS's moment of inertia in units of $10^{45}\,\mathrm{g\,cm^2}$, the spin frequency, $\nu_2 = \nu/100$ Hz, and the spin frequency derivative, $\dot{\nu}_{-14} = \dot{\nu}/10^{-14}\,\mathrm{Hz\,s^{-1}}$. We adopted a NS radius of 11 km, $\sin^2\theta \sim 0$–1, and $I_{45} = 1.5$, and obtained a magnetic dipole moment of $(9.8$–$13.4) \times 10^{26}\,\mathrm{G\,cm^3}$, corresponding to a relatively high surface magnetic field of $(7.3$–$10.4) \times 10^8$ G. Alternatively, if we adopted the spin frequency of $\nu_{2022} = 313.643\,740\,49(22)$ Hz that is reported in Sanna et al. (2022), we obtain a spin-down rate of $\dot{\nu} = (-4.08 \pm 0.81) \times 10^{-14}\,\mathrm{Hz\,s^{-1}}$ and magnetic field of $(6.2$–$8.7) \times 10^8$ G. Both values are slightly smaller than the aforementioned ones.

Recently, Sanna et al. (2026) derived a smaller spin-down rate of $\dot{\nu} \approx -2.25 \times 10^{-14}\,\mathrm{Hz\,s^{-1}}$. While the choice of the 2022 baseline plays a role, the primary driver of this discrepancy is the difference in the 2025 spin frequency measurement: our EP value is lower than their XMM-Newton value ($\nu_{\mathrm{XMM}} = 313.643\,738\,44(34)$ Hz) by $\sim 1.6\,\mu$Hz. It implies a larger frequency drop over the 3-year baseline, and thus a faster spin-down rate, regardless of which 2022 solution is used as a reference. However, despite these differences in $\dot{\nu}$, the inferred magnetic field strength derived by Sanna et al. (2026) ($B \lesssim 10^9$ G) remains broadly consistent with our estimate.

5.2. The non-detection of radio pulsation

The radio behavior of MAXI J1957+032 during its X-ray quiescent phase was previously uncharacterized. One of the primary motivations for our work was to determine if this source activates as a radio pulsar once accretion halts, a fundamental question for any such system. The pulsar recycling scenario predicts that this transition should occur, but a robust theory of when or how is absent (see e.g., Papitto & de Martino 2022). The empirical evidence is also ambiguous: a rare class of transitional millisecond pulsars (tMSPs), such as IGR J18245–2452, cleanly demonstrates this state-switching behavior (Papitto et al. 2013). In contrast, the vast majority of the wider AMXP population has evaded detection in numerous deep radio pulsation searches, with notable non-detections including Aql X–1 (Burgay et al. 2003; Peng et al. 2025), XTE J0929–314 (Iacolina et al. 2009), as well as XTE J1751–305, XTE J1814–338, and SAX J1808.4–3658 (Iacolina et al. 2010; Patruno et al. 2017). Our observations aimed to establish for the first time whether MAXI J1957+032 behaves like a tMSP or like the majority of radio-quiet AMXPs.

Our deep search for radio pulsations from MAXI J1957+032 using FAST yielded a non-detection, for which we establish a 7σ upper limit on the flux density of 12.3 μJy. Given the substantial spin-down power of $\dot{E} = -4\pi^2 I \nu \dot{\nu} \approx 1.1 \times 10^{36}\,\mathrm{erg\,s^{-1}}$, the obtained upper limit of the flux density corresponds to a radio luminosity limit of $L_{\mathrm{radio}} < 2.87 \times 10^{26}\,\mathrm{erg\,s^{-1}}$ in 1.05–1.45 GHz at a maximum distance of 7 kpc (Ravi 2017). This implies a radio conversion efficiency of $\xi = L_{\mathrm{radio}}/\dot{E} < 2.8 \times 10^{-10}$. This efficiency is significantly lower than the typical range of 10^{-8}–10^{-5} observed for MSPs with comparable spin-down power (Szary et al. 2014), indicating that the non-detection is intrinsic to the source, not a result of insufficient instrumental sensitivity.

Several scenarios can explain this quietness of radio pulsation (see Peng et al. 2025, and references therein). The first is a purely geometric effect, whereby the pulsar's narrow radio beam never intersects our line of sight. While this is a valid consideration for any single object, it becomes a less tenable explanation when applied to the growing population of non-detections. In the future, as many more quiescent AMXPs are targeted by deep searches with highly sensitive instruments like FAST, we will be able to test this hypothesis statistically. If radio pulsations continue to be systematically absent across a large sample, the geometric beaming explanation can be ruled out. Another compelling explanation is that a low-level accretion continues even during the X-ray quiescent phase. Even in quiescence, if the system operates in the propeller regime or undergoes radio ejection, a significant amount of material can be expelled from the inner system but remains in the vicinity. This ongoing inflow of matter, however faint, can effectively quench the radio emission by providing enough plasma to either absorb the radio signal via free–free absorption, or, more fundamentally, to suppress the accelerating electric potentials within the magnetospheric gaps required to power the coherent emission mechanism.

Acknowledgements. We appreciate the referee for constructive comments and suggestions, which improved the manuscript. This work was supported by the Major Science and Technology Program of Xinjiang Uygur Autonomous Region (No. 2022A03013-3) and China's Space Origins Exploration Program. Z.S.L. and Y.Y.P. were supported by National Natural Science Foundation of China (12273030, 12103042), the science and technology innovation Program of Hunan Province (No. 2024JC0001). This work is supported by the China Manned Space Program with grant no CMS-CSST-2025-A13. This work made use of data from the *Insight*-HXMT mission, a project funded by China National Space Administration (CNSA) and the Chinese Academy of Sciences (CAS), and also from the High Energy Astrophysics Science Archive Research Center (HEASARC), provided by NASA's Goddard Space Flight Center. EP is a space mission supported by Strategic Priority Program on Space Science of Chinese Academy of Sciences, in collaboration with ESA, MPE and CNES. FAST is a Chinese national megascience facility, operated by National Astronomical Observatories, Chinese Academy of Sciences. The research is partly supported by the Operation, Maintenance and Upgrading Fund for Astronomical Telescopes and Facility Instruments, budgeted from the Ministry of Finance of China (MOF) and administrated by the Chinese Academy of Sciences (CAS).

References

Altamirano, D., Casella, P., Patruno, A., Wijnands, R., & van der Klis, M. 2008, ApJ, 674, L45
Arnaud, K. A. 1996, ASP Conf. Ser., 101, 17
Burgay, M., Burderi, L., Possenti, A., et al. 2003, ApJ, 589, 902
Campana, S., Stella, L., & Kennea, J. A. 2008, ApJ, 684, L99

Cao, X., Jiang, W., Meng, B., et al. 2020, Sci. China: Phys. Mech. Astron., 63, 249504
Chakrabarty, D., Jonker, P. G., & Markwardt, C. B. 2016, ATel, 9591, 1
Chen, Y., Cui, W., Han, D., et al. 2020a, SPIE Conf. Ser., 11444, 114445B
Chen, Y., Cui, W., Li, W., et al. 2020b, Sci. China: Phys. Mech. Astron., 63, 249505
Cherepashchuk, A. M., Molkov, S. V., Lutovinov, A. A., & Postnov, K. A. 2015, ATel, 7506, 1
De Falco, V., Kuiper, L., Bozzo, E., et al. 2017, A&A, 599, A88
Galloway, D. K., Morgan, E. H., Krauss, M. I., Kaaret, P., & Chakrabarty, D. 2007, ApJ, 654, L73
Gendreau, K. C., Arzoumanian, Z., Adkins, P. W., et al. 2016, SPIE Conf. Ser., 9905, 99051H
Harrison, F. A., Craig, W. W., Christensen, F. E., et al. 2013, ApJ, 770, 103
Hotan, A. W., van Straten, W., & Manchester, R. N. 2004, PASA, 21, 302
Iacolina, M. N., Burgay, M., Burderi, L., Possenti, A., & di Salvo, T. 2009, A&A, 497, 445
Iacolina, M. N., Burgay, M., Burderi, L., Possenti, A., & di Salvo, T. 2010, A&A, 519, A13
Jiang, P., Tang, N.-Y., Hou, L.-G., et al. 2020, Res. Astron. Astrophys., 20, 064
Kennea, J. A., Evans, P. A., Beardmore, A. P., et al. 2016, ATel, 9572, 1
Li, Z. S., Kuiper, L., Falanga, M., et al. 2021, A&A, 649, A76
Li, Z., Kuiper, L., Ge, M., et al. 2023, ApJ, 958, 177
Li, Z. S., Kuiper, L., Pan, Y. Y., et al. 2024, A&A, 691, A92
Li, Z., Kuiper, L., Pan, Y., et al. 2025a, ApJ, 990, 15
Li, Z., Kuiper, L., Pan, Y. Y., et al. 2025b, ATel, 17279, 1
Liu, C., Zhang, Y., Li, X., et al. 2020, Sci. China: Phys. Mech. Astron., 63, 249503
Mata Sánchez, D., Charles, P. A., Armas Padilla, M., et al. 2017, MNRAS, 468, 564
Molkov, S. V., Lutovinov, A. A., Postnov, K. A., & Cherepashchuk, A. M. 2015, ATel, 7520, 1
Negoro, H., Serino, M., Mihara, T., et al. 2015, ATel, 7504, 1
Negoro, H., Iwakiri, W., Kawakubo, Y., et al. 2022, ATel, 15440, 1
Negoro, H., Nakajima, M., Takagi, K., et al. 2025, ATel, 17170, 1
Papitto, A., & de Martino, D. 2022, Astrophys. Space Sci. Lib., 465, 157
Papitto, A., Ferrigno, C., Bozzo, E., et al. 2013, Nature, 501, 517
Patruno, A., Jaodand, A., Kuiper, L., et al. 2017, ApJ, 841, 98
Peng, L., Li, Z., Pan, Y., et al. 2025, ApJ, 983, 44
Ransom, S. M. 2001, Ph.D. Thesis, Harvard University, Massachusetts, USA
Rau, A., Yates, R., & Greiner, J. 2015, ATel, 7524, 1
Ravi, V. 2017, ApJ, 851, 114
Riggio, A., Burderi, L., di Salvo, T., et al. 2011, A&A, 531, A140
Sanna, A., Bult, P., Ng, M., et al. 2022, MNRAS, 516, L76
Sanna, A., Illiano, G., Baglio, M. C., et al. 2026, A&A, 706, A204
Spitkovsky, A. 2006, ApJ, 648, L51
Sugimoto, J., Negoro, H., Sugizaki, M., et al. 2015, ATel, 8143, 1
Sun, H., Zhang, M. H., Cheng, H. Q., et al. 2025, GCN, 40375, 1
Szary, A., Zhang, B., Melikidze, G. I., Gil, J., & Xu, R.-X. 2014, ApJ, 784, 59
Tanaka, K., Negoro, H., Ueno, S., et al. 2016, ATel, 8529, 1
van den Eijnden, J., Fender, R., Woudt, P., Miller-Jones, J., & Motta, S. 2022, ATel, 15462, 1
van Leeuwen, J., & Stappers, B. W. 2010, A&A, 509, A7
Wilms, J., Allen, A., & McCray, R. 2000, ApJ, 542, 914
Yuan, W., Dai, L., Feng, H., et al. 2025, Sci. China: Phys. Mech. Astron., 68, 239501
Zhang, S.-N., Li, T., Lu, F., et al. 2020, Sci. China: Phys. Mech. Astron., 63, 249502
Zhao, X., Cui, W., Wang, H., et al. 2025, RAA, 25, 015002